



Effects specific surface area and oxygen vacancy on the photocatalytic properties of mesoporous F doped SnO₂ nanoparticles prepared by hydrothermal method

Xiaolong Wang^{1,2} · Min Xu¹ · Lu Liu¹ · Yan Cui¹ · Hansong Geng¹ · Hongli Zhao¹ · Bo Liang¹ · Jingkai Yang¹ 

Received: 7 May 2019 / Accepted: 3 August 2019 / Published online: 16 August 2019
© Springer Science+Business Media, LLC, part of Springer Nature 2019

Abstract

Mesoporous Fluorine doped SnO₂ (FTO) nanoparticles (NPs) have been successfully synthesized by hydrothermal process. Subsequent annealing process at 350 °C, 500 °C, 650 °C and 800 °C has been carried out to synthesize FTO photocatalysts with different specific surface areas and oxygen vacancy contents. X-ray diffraction (XRD), transmission electron microscopy (TEM), Raman spectroscopy characterization, Raman measurement, X-ray photoelectron spectroscopy (XPS), Brunauer–Emmett–Teller (BET), X-ray photoelectron spectroscopy (XPS), UV–Vis diffuse reflectance and Photoluminescence (PL) spectra have been used to investigate the effects of specific surface areas and oxygen vacancy contents on the photocatalytic properties of mesoporous FTO photocatalysts. The results show that the mesoporous FTO NPs consist of spherical nanoparticles of 3–6 nm in diameters with a tetragonal crystal structure. The as-synthesized mesoporous FTO NPs with the band gap of 3.91 eV, the largest number of oxygen vacancies and the largest surface area of 145.55 m² g⁻¹ exhibit an excellent photocatalytic activity when degrading methyl orange (MO) under UV light irradiation, and the degradation of dye methyl orange (MO) can reach 97% within 80 min. Moreover, the superoxide oxide ($\bullet\text{O}_2^-$) is the major active specie, which has played a key role in MO degradation system. The photocatalytic mechanism of FTO photocatalysts has been also proposed.

1 Introduction

Tin oxide (SnO₂) is one of the most widely-used metal oxide semiconductor materials applied in gas sensors, lasers diodes, solar cells, transparent conductors, light-emitting diodes, fluorescent materials photocatalyst and so on [1–5], because of its excellent low electrical resistance and high optical transparency. Recently, SnO₂ has attracted great

interests in the photocatalytic degradation of environmental pollutants, due to its efficient photoactivity, low cost, least toxic, low electrical resistance, and stability against thermal and chemical environments [6–8]. However, SnO₂ exhibits poor photocatalytic activity due to its wide band-gap (3.6 eV), low generation efficiency and rapid combination of electron–hole pairs in photocatalytic reaction [9, 10].

To address these, many researchers have paid attention to tuning the photocatalytic properties of SnO₂ by doping with ions or constructing semiconductor heterojunction with other oxide to improve the photocatalytic performance [11–15]. Among the doped SnO₂ materials, fluorine doped SnO₂ (FTO) materials exhibit superior chemical and thermal stability, higher hardness and lower cost [16]. Moreover, F doping could engineer the band gap and modify the photoelectric properties of SnO₂ due to the similar ionic radius of F⁻ ($\approx 1.33 \text{ \AA}$) and O²⁻ ($\approx 1.40 \text{ \AA}$). As is known, the photocatalytic properties strongly depend on the particle sizes, morphology, defects and band gaps [17–19]. Doping SnO₂ can also generate defects in the crystal lattice and create oxygen vacancies, which significantly help to improve photocatalytic properties, and smaller particle size is highly favorable for increasing the photocatalytic efficiency [20,

Electronic supplementary material The online version of this article (<https://doi.org/10.1007/s10854-019-01981-y>) contains supplementary material, which is available to authorized users.

✉ Bo Liang
liangbo@ysu.edu.cn

✉ Jingkai Yang
yangjkysu@163.com

¹ State Key Laboratory of Metastable Materials Science and Technology, College of Materials Science and Engineering, Yanshan University, Qinhuangdao 066004, China

² Division of Functional Materials and Nano Devices, Ningbo Institute of Material Technology and Engineering, Chinese Academy of Sciences, Ningbo 315201, China

21]. A number of studies have been reported on the structural, optical and photocatalytic properties of FTO thin films in the past few decades [22, 23]. However, to the best of our knowledge, a very limited number of reports were dedicated to the study of the photocatalytic activity of FTO NPs under UV light irradiation.

As is known, high photocatalytic properties depend on the high surface-to-volume ratio with local disorders, defects and vacancy clusters on the surfaces. Herein, in this work, mesoporous FTO NPs with high surface-to-volume ratios were prepared by hydrothermal method, and the photocatalytic activity was evaluated for the degradation of methyl orange (MO) under UV light. The microstructural and photocatalytic properties of mesoporous FTO NPs have been investigated to propose a schematic diagram for energy band structure with photocatalytic process.

2 Experimental procedure

2.1 Synthesis of FTO NPs

In this work, FTO NPs were synthesized by hydrothermal process. Tin chloride pentahydrate ($\text{SnCl}_4 \cdot 5\text{H}_2\text{O}$) and ammonium fluoride (NH_4F) were used as the starting material and F dopant source, respectively. All of the raw materials were used without further purification. Firstly, 14.024 g $\text{SnCl}_4 \cdot 5\text{H}_2\text{O}$ was dissolved into 75 mL deionized water mixed with 75 mL ethanol ($\text{C}_2\text{H}_5\text{OH}$) and 2 mL concentrated hydrochloric acid (HCl : 36 wt% \leq concentration \leq 38 wt%). Secondly, 0.741 g NH_4F (F/Sn = 50 at. % in the precursor solution [24]) was added to the above solution under stirring. After that, concentrated ammonia ($\text{NH}_3 \cdot \text{H}_2\text{O}$) was added into the above solution to adjust pH to 2.0. The mixed solution was stirred magnetically for 4 h to obtain homogenous precursor solution. Thirdly, the mixed solution was transferred into the 200 mL Teflon-sealed autoclave and held at 180 °C for 12 h. After that, the obtained precipitation was filtered and washed with distilled water and alcohol several times to remove impurities completely, then dried at 80 °C for 4 h, and then grounded into powders for annealing. Finally, the powders were annealed for 0.5 h in a muffle furnace to obtain FTO NPs. The annealing temperature was designed as 350 °C, 500 °C, 650 °C and 800 °C.

2.2 Sample characterizations

The crystal structure of the as-synthesized and annealed FTO NPs with different annealing temperatures was determined by X-ray diffraction (XRD, D/max-2500PC diffractometer, Rigaku, Tokyo, Japan) with $\text{Cu-K}\alpha$ radiation ($\lambda = 0.15406$ nm). Selected area electron diffraction (SAED), high resolution transmission electron microscopy (HRTEM)

images were performed by transmission electron microscopy (TEM, JEM-2010 spectrometer, JEOL, Tokyo, Japan). The Raman spectroscopy was carried out by a Renishaw 2000 in via Raman spectrometer (London, UK). The specific surface areas of samples were determined with a surface-area analyzer (TriStar II Plus 2.02, Micromeritics, USA) by the Brunauer–Emmett–Teller (BET) method based on the nitrogen adsorption isotherm, while the pore size distribution was estimated by Barrett–Joyner–Halenda (BJH) theory. UV–Vis spectrometer (UV-3150, Shimadzu, Kyoto, Japan) was taken to record Diffuse reflectance spectra (DRS) using BaSO_4 as a reference. Chemical composition and the various elements chemical state were investigated by X-ray photoelectron spectroscopy (XPS, SCIENTIFIC ESCALAB 250 Xi spectrometer, Thermo, Waltham, MA, USA). Al K α was used as the excitation source with X-rayspot size of 0.25 mm. Photoluminescence (PL) performance was obtained by a Hitachi F-2500 fluorescence spectrophotometer at room temperature. Particle size was determined by dynamic light scattering (DLS) using a Zetasizer Nano ZS (Malvern Instruments, UK). The Mott–Schottky plots of the prepared photoelectrodes were measured in 0.1 mol L⁻¹ Na_2SO_4 solution using a CHI660D electrochemical workstation. The measurements were performed using a three-electrode configuration. The prepared photoelectrode, Ag/AgCl (saturated KCl) electrode and Pt electrode were acted as the working, reference and counter electrodes, respectively. The working electrode was prepared as follows: Firstly, 10 mg catalyst sample was mixed with 50 μL Nafion solution and the 1 mL ethanol under ultrasound. Then, the above solution was dropped on fluorine-doped tin oxide conducting glass (2 cm \times 1.5 cm). At last, the electrode was calcined at 70 °C for 1 h.

2.3 Photoalytic activity of FTO NPs

The reduction of dye methyl orange (MO) was degraded under UV light to study the photocatalytic activity of the as-synthesized and annealed FTO NPs with different annealing temperatures. The photocatalytic device (XPA-7 (G5), Xujiang Electromechanical plant, Nanjing, China) was used to provide a stable ambient environment, and a 300 W mercury lamp with a 420-nm cut-off filter (JB420) was used as a UV light source to trigger the photocatalytic reaction. 100 mg of FTO photocatalyst was added to an aqueous solution of methyl orange (100 mL, 20 ppm).

Prior to irradiation, the dye solution was stirred for 30 min in the dark to ensure adsorption–desorption equilibrium between the dye solution and the photocatalyst. After a certain time, 3.0 mL aliquots were withdrawn from the photoreactor and centrifuged to remove the catalyst. The concentration of the dye during the photoreaction were recorded by an UV–Vis spectrometer in a scanning range of 200 ~ 700 nm at room temperature. Several consecutive

reaction rounds were measured to determine the stability of the catalyst. To confirm that the photocatalytic activity is due to the photocatalyst only, we carried out blank experiments without a catalyst under light (photolysis) with a catalyst in the dark (adsorption).

3 Results and discussion

3.1 XRD analysis

The XRD patterns of the as-synthesized and annealed FTO NPs with different annealing temperatures are shown in Fig. 1. Each sample exhibits a pure tetragonal rutile phase of SnO₂ according to PDF#71-0652, regardless of annealing condition. The broader peaks of the as-synthesized sample infer to a lower crystallinity. The peaks become sharper with increasing annealing temperature, indicating a gradual increase in the average grain size and enhancement of crystallinity. The grain sizes calculated according to the Debye–Scherrer formula are listed in Table 1. It could

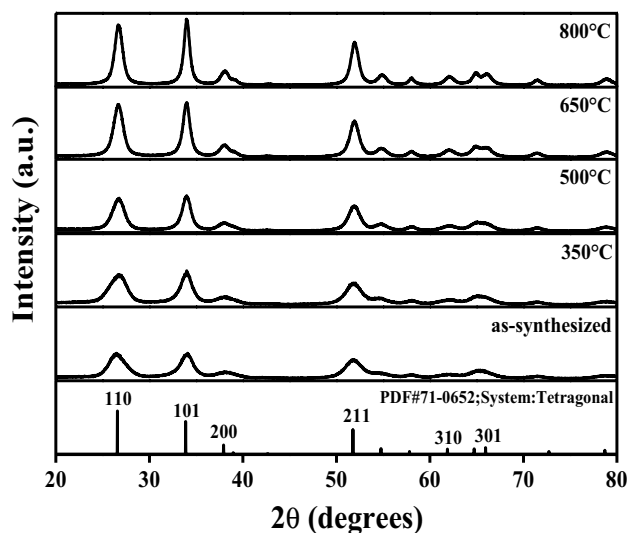


Fig. 1 XRD patterns of the as-synthesized and annealed FTO NPs with different annealing temperature

Table 1 XRD patterns of the as-synthesized and annealed FTO NPs with different annealing temperature

Samples	D-spacing			Lattice parameters			D (nm)
	d ₁₁₀ (Å)	d ₁₀₁ (Å)	d ₂₁₁ (Å)	a (Å)	c (Å)	v (Å ³)	
PDF#71-0652	3.35	2.644	1.764	4.738	3.187	71.5	–
As-synthesized	3.366	2.621	1.765	4.773	3.136	71.457	4.58
350 °C	3.330	2.635	1.763	4.744	3.168	71.304	6.33
500 °C	3.326	2.635	1.760	4.732	3.172	71.017	8.25
650 °C	3.343	2.635	1.759	4.726	3.174	70.871	10.63
800 °C	3.341	2.638	1.758	4.718	3.181	70.817	15.06

be seen that the grain size gradually increases from about 4.58 nm to 15.06 nm with the increasing annealing temperature. What is more, the interplanar spacing (D-spacing) and lattice parameters calculated from the XRD spectra increase with annealing temperature, which is due to the growth of particles size that reduces grain boundaries where the severe lattice dislocation decreases the interaction of atoms and increases the lattice parameters.

3.2 Microstructure analysis

The TEM images, SAED patterns and HRTEM images in Fig. 2 show the changes in morphologies of the as-synthesized and annealed FTO NPs with different annealing temperatures. From the TEM images, it is evident that the as-synthesized FTO NPs are considerably agglomerated and polycrystalline in nature. Subsequent annealing treatment decreases the agglomeration and disperses the grain particles. The spherical particles could be seen in all samples with gradually increase of grain size from about 3 to 20 nm with the increasing annealing temperature. What is more, in the case of samples annealed at 650 °C and 800 °C (Fig. 2d, e), some rod-like structures can be seen with 45 nm in length and 9 nm in width, and 80 nm in length and 12 nm in width, respectively. These rod-like structures further decrease the agglomeration. The diffraction rings of the inserted SAED pattern from inside to outside can be respectively indexed to (110), (101), (211) and (310) planes of tetragonal SnO₂, which matches well with the XRD pattern. In addition, the homologous SAED patterns show gradually discontinuous diffraction rings instead of shiny circles at higher annealing temperature, and it indicates the gradual increase of grain size. The subsequent HRTEM images further revealed that the FTO NPs are all of high crystallinity. The interplanar spacing as calculated from the HRTEM images are 0.34 nm, 0.26 nm and 0.18 nm which correspond to (110), (101) and (200) lattice planes, respectively.

3.3 Raman analysis

Raman scattering can be used to understand the crystallinity, structural defects and size effects of nanoscale crystallites

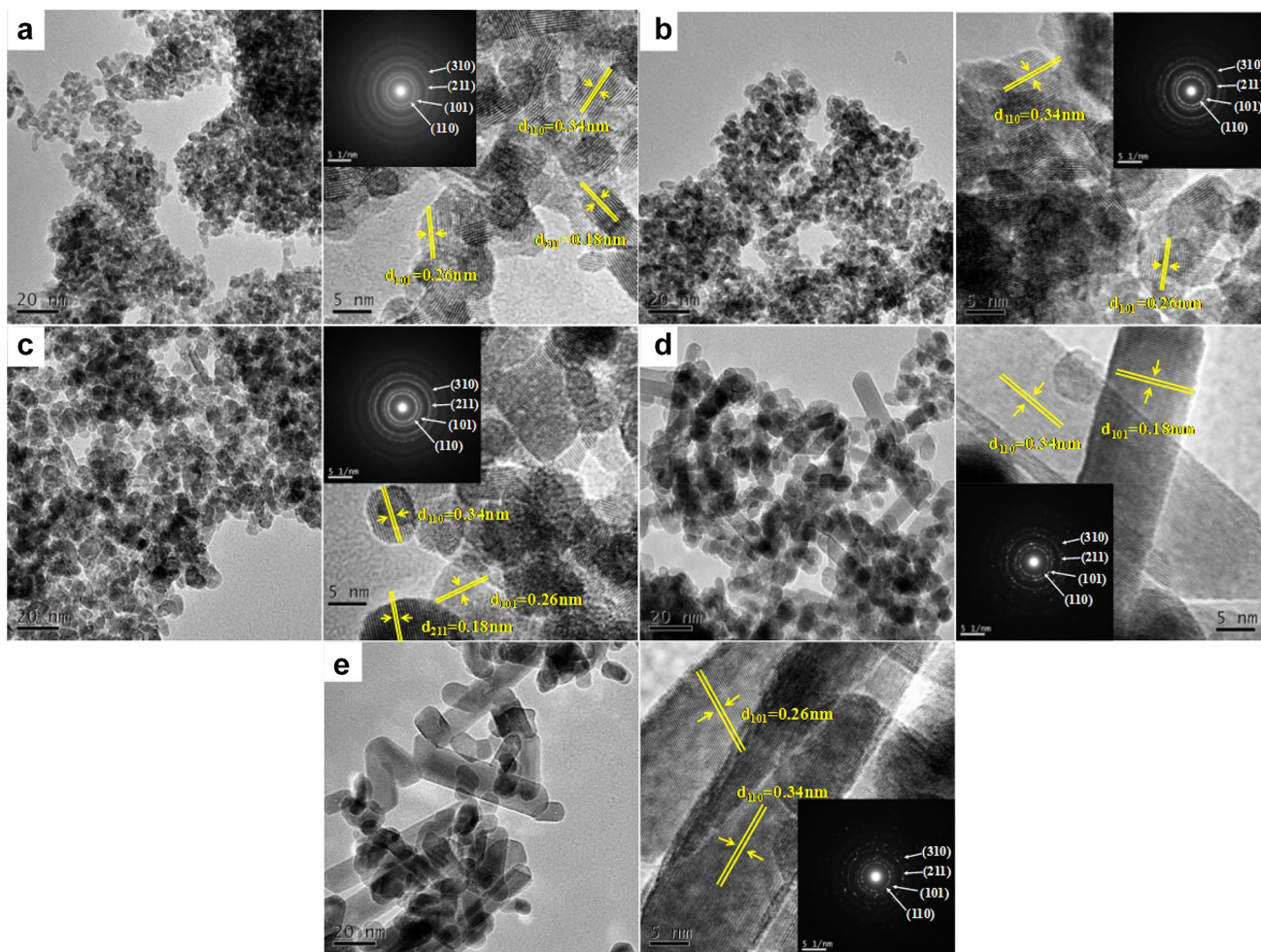


Fig. 2 Transmission electron micrograph (TEM) images, high resolution transmission electron microscopy (HRTEM) and selected area electron diffraction (SAED) pattern of the as-synthesized and annealed FTO NPs with different annealing temperature: **a** as-synthesized FTO NPs; **b** FTO NPs annealed at 350 °C; **c** FTO NPs annealed at 500 °C; **d** FTO NPs annealed at 650 °C; **e** FTO NPs annealed at 800 °C

ized FTO NPs; **b** FTO NPs annealed at 350 °C; **c** FTO NPs annealed at 500 °C; **d** FTO NPs annealed at 650 °C; **e** FTO NPs annealed at 800 °C

on vibrational properties. The SnO₂ has a unit cell that consists of two tin and four oxygen atoms. The 6 unit cell atoms give a total of 18 branches for the vibration modes in the first Brillouin’s zone. The mechanical representation of the normal vibration modes at the center of the Brillouin’s zone is given as: $\Gamma = A_{1g} + A_{2g} + B_{1g} + B_{2g} + E_g + A_{2u} + 2B_{1u} + 3E_u$. The A_{2g} and B_{1u} are neither Raman active nor infrared active (IR). The symmetrical A_{2u} and E_u modes are IR active, whereas the remaining A_{1g} , B_{1g} , B_{2g} and E_g modes are Raman active and they are also fundamental vibrational modes in pure SnO₂.

Figure 3 shows the evolution of Raman spectra of FTO NPs, and these spectra confirm the characteristics of the tetragonal rutile structures [25]. The detected Raman peaks of FTO NPs at 630 cm⁻¹ and 773 cm⁻¹ correspond to A_{1g} and B_{2g} , which both vibrate in the plane perpendicular to the *c*-axis and correspond to the asymmetric stretching of Sn–O

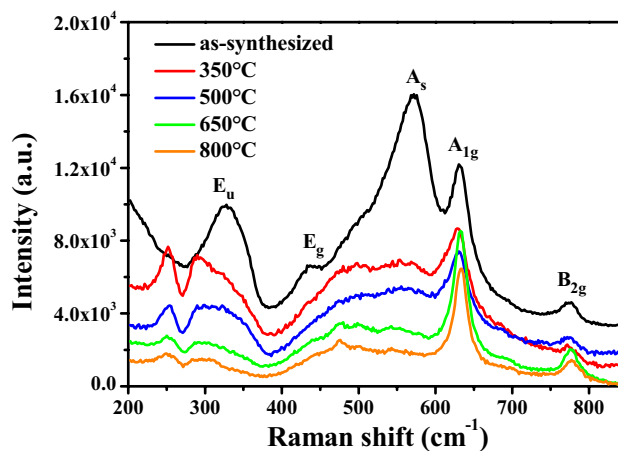


Fig. 3 Raman spectra of the as-synthesized and annealed FTO NPs with different annealing temperature

bonds. Due to the fact that A_{1g} and B_{2g} are sensitive to the grain size, the increase of intensity along with blue shifts of A_{1g} and B_{2g} peaks could be attributed to the increase of grain size with increasing annealing temperature, as confirmed by HRTEM and XRD.

The Raman peak at 477 cm^{-1} corresponds to E_g mode, which vibrates in the opposite direction of the c -axis through two oxygen atoms. In addition, a broad peak within $270\text{--}380\text{ cm}^{-1}$ region of spectra which indicates the amorphous and nanocrystalline nature of the samples is attributed to the E_u mode [26]. In the nanocrystalline SnO_2 system, E_g mode, E_u mode as well as two peaks located at 251 cm^{-1} and 571 cm^{-1} are sensitive to not only to grain size but also to surface imperfections. As the fact that surface imperfections such as local disorder, surface defects (especially oxygen defects) and vacancy cluster could be easily generated on as-synthesized FTO NPs surface, the decreasing intensity of four peaks with increasing temperature could be attributed to the reduction of specific surface area and the conversion from amorphous to crystalline, both of which reduce the surface imperfections.

3.4 BET analysis and DLS analysis

The importance of surface area to photocatalysis derives from the ability of a larger surface area to provide more active sites for the adsorption of reagent molecules. In this work, BET surface areas and pore size distributions were determined for FTO NPs by measuring nitrogen adsorption–desorption isotherms. Figure 4 shows the BET surface area (Fig. 4a) and pore diameter (Fig. 4b). The N_2 adsorption isotherm of FTO NPs at room temperature displayed type IV behavior and distinct H_2 type hysteresis loops, signifying the mesoporous feature of synthesized materials. The values of BET surface area, pore diameter and volume were given in Table 2. It is noted that the calculated BET surface

Table 2 BET N_2 adsorption surface area of the as-synthesized and annealed FTO NPs with different annealing temperatures

Samples	BET N_2 surface area ($\text{m}^2\text{ g}^{-1}$)	Pore diameter (nm)	Pore volume ($\text{cm}^3\text{ g}^{-1}$)
As-synthesized	145.55	4.41	0.161
350 °C	129.34	5.17	0.167
500 °C	74.95	8.77	0.164
650 °C	44.86	14.05	0.158
800 °C	38.84	17.00	0.165

area decreases with increasing annealing temperature, while the pore diameter increases. The minished surface area of FTO NPs provides less active sites, which will decrease the photocatalytic performance with less absorption of reactant molecules.

Dynamic light scattering (DLS) was used to determine the size distribution of particles in solutions. The results are shown in Fig. 5. Mean particles sizes were estimated at 657.9, 558.2, 702.3, 747.8 and 960.2 nm for as-synthesized FTO NPs; FTO NPs annealed at 350 °C, FTO NPs annealed at 500 °C, FTO NPs annealed at 650 °C, FTO NPs annealed at 800 °C, respectively. The particle size of FTO NPs annealed at 350 °C is lower than that of the as-synthesized samples due to the decomposition of precursor [27]. What is more, the particle size of FTO NPs increases with increasing annealing temperature. This result can be attributed to the fact that the increasing annealing temperature of FTO NPs leads to a high agglomeration of nanoparticles.

3.5 UV–Vis diffuse reflectance analysis

The UV–Vis diffuse reflectance spectra of the as-synthesized and annealed FTO NPs with different annealing temperatures are shown in Fig. 6. All the samples present

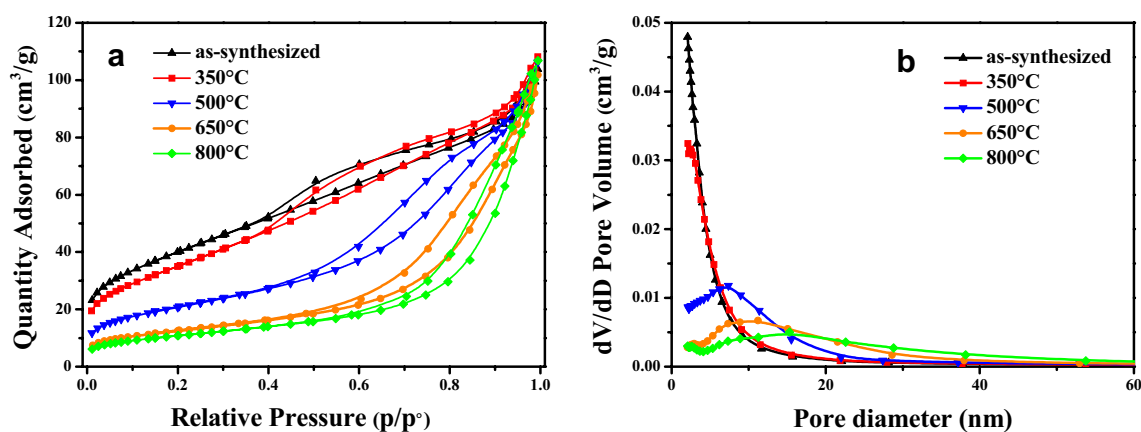


Fig. 4 **a** N_2 adsorption/desorption isotherm of the as-synthesized and annealed FTO NPs with different annealing temperature; **b** Pore size distribution data of the as-synthesized and annealed FTO NPs with different annealing temperature

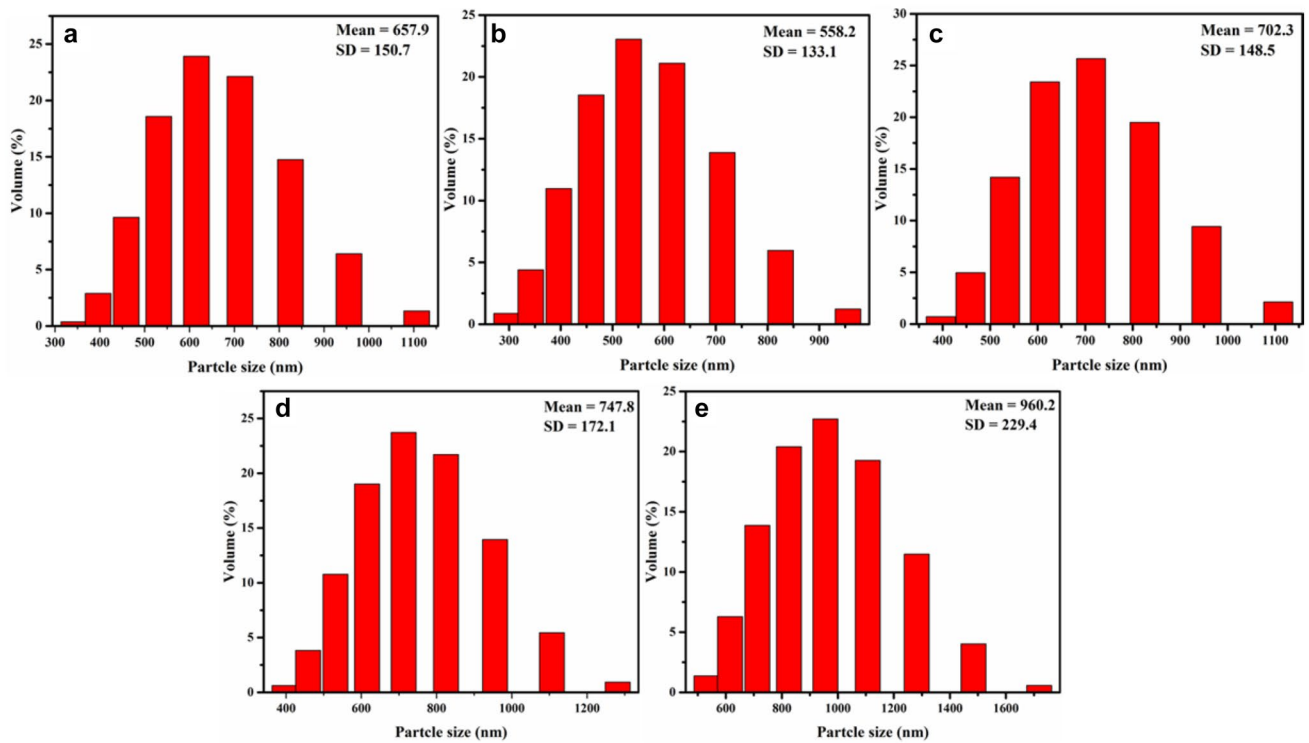


Fig. 5 Particle size distribution histograms of **a** as-synthesized FTO NPs; FTO NPs annealed at **b** 350 °C; **c** 500 °C; **d** 650 °C; **e** 800 °C

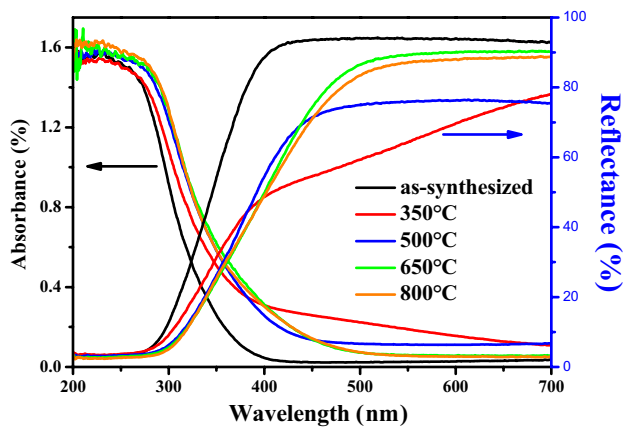


Fig. 6 The UV-vis diffuse reflectance spectra of the as-synthesized and annealed FTO NPs with different annealing temperature

a good optical quality in the UV region since the strong absorbance and complete reflectance in the 200–280 nm range. The band gap energy (E_g) values of the as-synthesized and annealed FTO NPs with different annealing temperatures were done by extrapolating the linear part of $h\nu$ versus $(\alpha h\nu)^2$ graph to the x axis according to Tauc equation [28], as shown in Fig. 7. The E_g values (as shown in the inset of Fig. 7) of all the samples are larger than that of bulk SnO_2 (3.6 eV) and decrease from

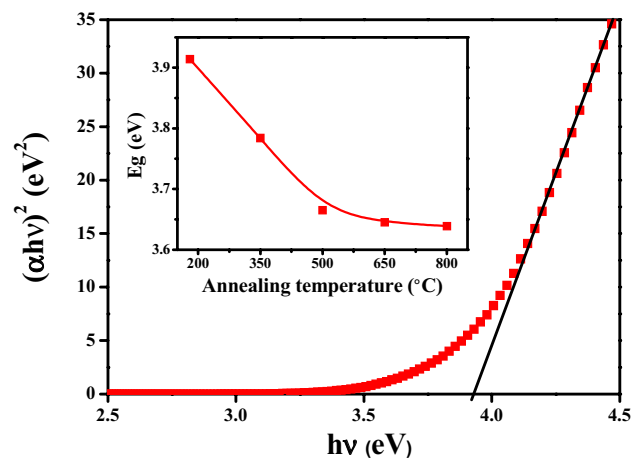


Fig. 7 Plot of $(\alpha h\nu)^2$ versus photon energy ($h\nu$) of the as-synthesized and annealed FTO NPs with different annealing temperature (insert is band-gap evolution as a function of annealing temperature)

3.91 to 3.67 eV with the increase of annealing temperature. Moss-Burstein effect is also counts, as the annealing process decreases the carrier concentration, which lower the Fermi level in the conduction band. The red shift of the absorption edges and reflection edges with increasing annealing temperature is also due to the quantum confinement effect [29].

3.6 Photocatalytic performance and carrier concentration

The evolutions of UV–Vis absorption spectra of dye methyl orange (MO) photodegradation under the irradiation of under UV light over the as-synthesized and annealed FTO NPs with different annealing temperatures are shown in Fig. 8, respectively. Before irradiation, the maximum absorption band for the MO is at 464 nm and show blue shifts in the presence of FTO NPs comparing the original MO absorption spectrum with the one after dark treatment for 30 min, which is due to the quantum size effect that

widens the band gap of the semiconductors [30]. When the annealing temperature increases, the absorption spectrum after dark treatment shows a red shift trend.

Further, Fig. 9a shows the photocatalytic degradation curves of the as-synthesized and annealed FTO NPs with different annealing temperatures, respectively. For comparison, blank experiment (without catalyst) is also performed. It can be seen that the concentration of MO barely changes under the UV light irradiation without catalyst. The maximum absorption intensity decreases rapidly and almost disappears after 80 min irradiation in the present of FTO NPs, indicating that the chromophoric structures are destroyed.

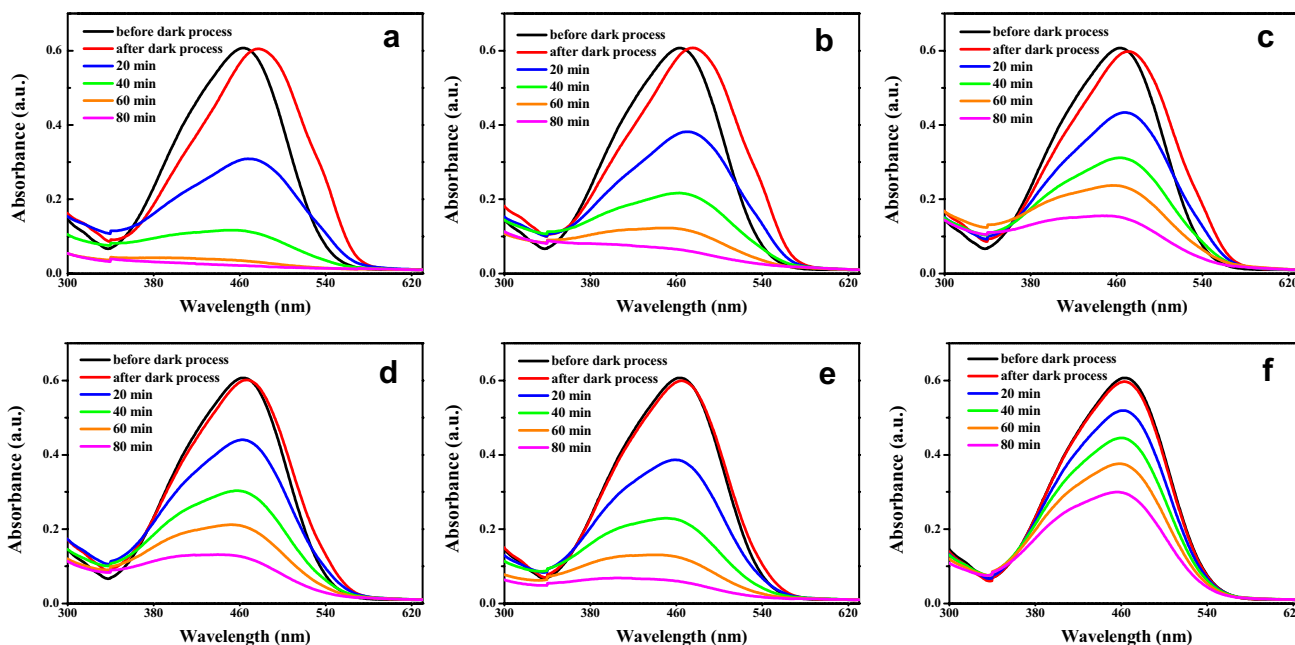


Fig. 8 UV–Vis absorbance of MO during photocatalytic degradation under UV–Vis irradiation with photocatalyst: **a** as-synthesized FTO NPs; **b** FTO NPs annealed at 350 °C; **c** FTO NPs annealed at 500 °C; **d** FTO NPs annealed at 650 °C; **e** FTO NPs annealed at 800 °C; **f** no photocatalyst

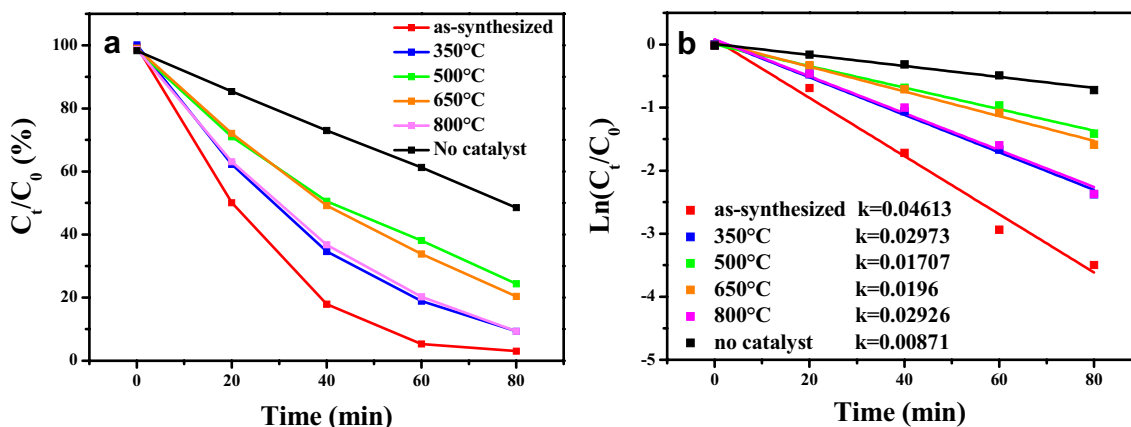


Fig. 9 **a** Photodegradation efficiency of MO over the as-synthesized and annealed FTO NPs with different annealing temperature; **b** Photodegradation kinetics of MO by means of plotting $\ln(C_t/C_0)$ versus time

The degradation efficiency of the as-synthesized FTO NPs is 97% after 80 min irradiation. The first kinetic-order constant (k) of MO degradation over FTO NPs is investigated as shown in Fig. 9b, and the variation of k with annealing temperature is presented in the picture. According to the kinetic analysis, the highest kinetic rate constant is estimated in the as-synthesized samples. What is more, the k value of FTO NPs annealed at 500 °C is the lowest, which means that FTO NPs annealed at 500 °C possesses the poorest photocatalytic efficiency among all samples.

In order to analyze the carrier concentration and the type of as-synthesized FTO NPs, Mott-Schottky plots were performed. According to the following equation:

$$1/C^2 = (2/\epsilon\epsilon_0eN_d)[(E - E_{FB}) - KT/e]$$

where, C is the capacitance of the space charge region in the semiconductor; N_d is the carrier concentration, e is the elemental charge, ϵ_0 is the permittivity of free space, ϵ is the relative permittivity of the semiconductor, E is the applied potential, E_{FB} is the flat band potential, T is the temperature,

and K is the Boltzmann constant. Figure S1 shows a negative slope for as-synthesized FTO NPs, indicating that the as-synthesized FTO NPs exhibit n-type behavior with electrons as the major carriers. Moreover, the N_d can be calculated from the slope of Mott-Schottky plot, and the carrier concentration of the as-synthesized FTO NPs is estimated as $2.61 \times 10^{16} \text{ cm}^{-3}$.

3.7 XPS analysis

The typical XPS binding energy spectra for Sn3d, O1s and F1s core levels of the as-synthesized and annealed FTO NPs with different annealing temperature are shown in Fig. 10, using C1s peak at 284.8 eV as the reference point for charge correcting. The separation of 8.45 eV between the Sn3d_{5/2} and Sn3d_{3/2} levels confirms the chemical state of Sn⁴⁺ in SnO₂ [31]. The asymmetry of O1s peaks shows more than one kind of chemical states of oxygen. Further, the small negative chemical shifts in O1s and Sn3d binding energies with increasing annealing temperature ascribes

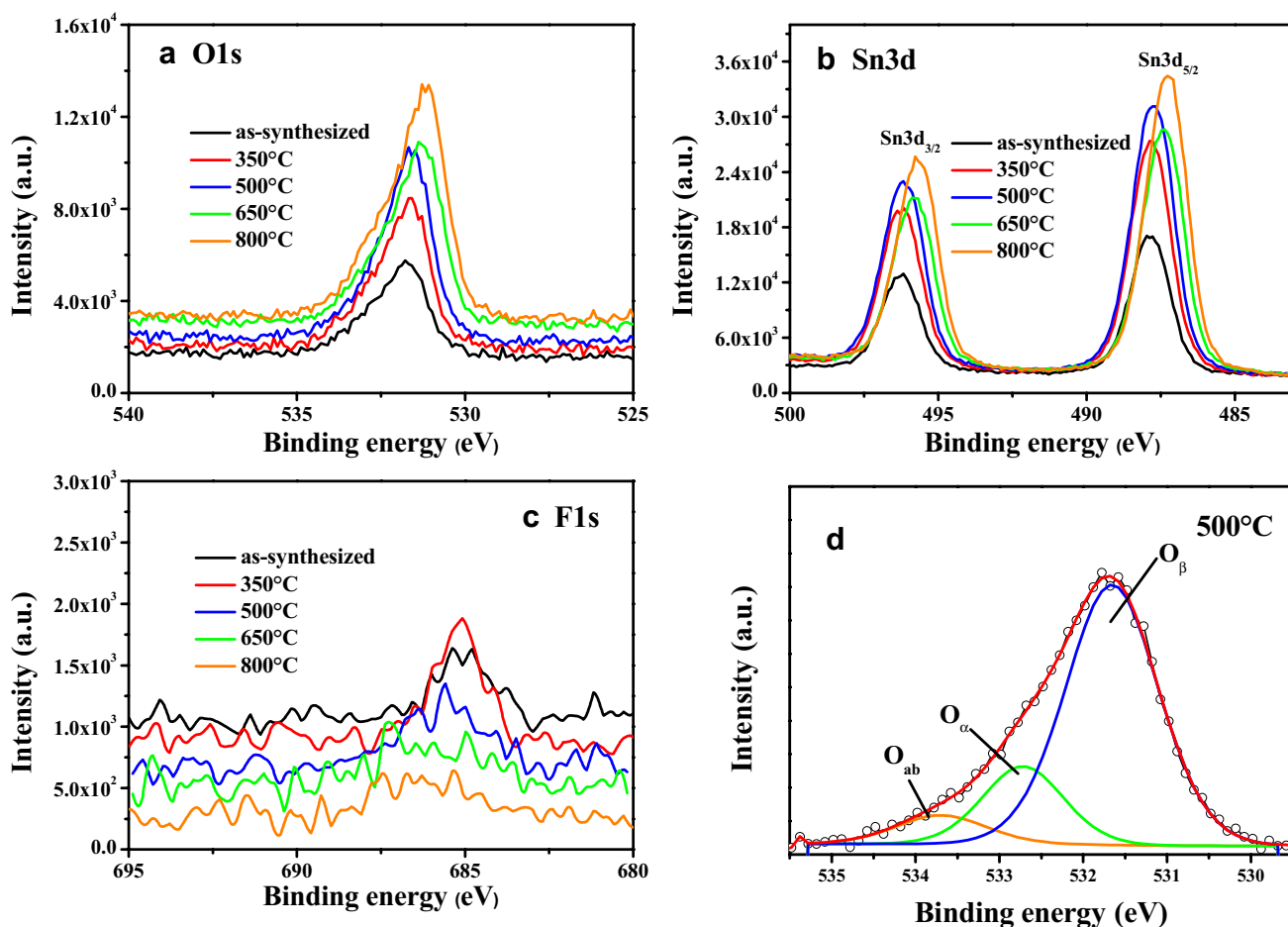


Fig. 10 XPS spectra of the as-synthesized and annealed FTO NPs with different annealing temperature: **a** O1s; **b** Sn3d; **c** F1s; and **d** Gaussian deconvoluted O1s spectrum of the FTO NPs annealed at 500 °C

to the incorporation of O^{2-} into the SnO_2 lattice, which may decrease the concentration of oxygen vacancies [32]. A slight positive chemical shift in F1s binding energies observed at higher annealing temperature may be due to the substitution of O^{2-} into F in the SnO_2 lattice.

Further, the core level spectra of O1s in the FTO NPs were fitted utilizing a Gaussian function and classified into three types of oxygen chemical states, and the deconvoluted O1s in FTO NPs annealed at 500 °C is presented in Fig. 10d. The lowest binding energy O_{ab} peak can be related to the chemisorbed oxygen species on the surface of FTO NPs. The medium binding energy O_{α} peak can be assigned to the oxygen vacancies in the oxygen deficient regions. The intensity of the O_{α} peak is an indication of the concentration of oxygen defects (V_O^0, V_{+O}, V_{++O}) in FTO NPs. The highest binding energy O_{β} peak can be attributable to the O^{2-} ions in the tetragonal rutile structure of SnO_2 . The relative content and peak position of the three kinds of oxygen chemical states are listed in Table 3.

The relative content of O_{α} peaks provides a view of the variation of oxygen vacancies concentration with different annealing temperature. It signifies that highly content of the O_{α} peak takes place in the as-synthesized sample, and reduces from 16.19% to 13.15% with increase in annealing temperature. This phenomenon can be explained as follows: annealing treatment provides energy for oxygen in the air to occupy the oxygen-deficient lattice sites in FTO NPs, which releases charge imbalance and lattice distortion, and regulates the lattice order. Therefore concentration of oxygen vacancies decreases, finally [24, 33]. Photoluminescence analysis will confirm this trend, as the defects are responsible for the UV-blue emission in FTO NPs [34].

3.8 Photoluminescence analysis

The room-temperature PL spectra the as-synthesized and annealed FTO NPs with different annealing temperatures under the wavelength excitation of 255 nm are shown in Fig. 11a. Intense emission in the range of 350–500 nm with a shoulder peak at 550 nm was observed. For detail exploration of the photoluminescence spectra, all spectra have been deconvoluted into eight strong emission bands along with many weak emission peaks following Gaussian fitting, and all samples exhibit similar type of PL Gaussian peaks, demonstrating that annealing process has not induced any kind of new PL phenomena. The deconvoluted spectrum of the as-synthesized FTO NPs is shown in Fig. 11b. What is more, taking the intensity of Peak 8 as the contrast, the intensity changes of all peaks are given in Fig. 12, using the formula $(I_k/I_{k0})/(I_8/I_{80})$, where I_k is the intensity of the Peak 1–8 of the samples at different annealing temperature, I_{k0} is the intensity of the Peak 1–8 of the as-synthesized sample, I_8 is the intensity of P8 of the samples at different annealing temperature and I_{80} is the intensity of the Peak 8 of the as-synthesized sample. In the case of the UV-blue region, the emission intensity drops rapidly with increase in annealing temperature, and the green-red region have almost the same ones ($I_b/I_g > 0.82$).

Since the energies corresponding to all emissions are found to be lower than the optical band gap (~ 3.8 eV), therefore the PL emission could be attributed to the defect energy states located within the band gap [35, 36]. In general, the oxygen vacancies are the most common defects in SnO_2 nanostructured materials and are used to be the radiative centers in the luminescence process. The possible

Table 3 Binding energy, peak position and the relative content of Gaussian peaks and relative content of O1s of the as-synthesized and annealed FTO NPs with different annealing temperatures

Sample	O1s Relative content (at. %)	Gaussian peak	Peak position (eV)	Area (%)	O_{α} (at. %)
As-synthesized	65.26	O_{ab}	532.21	18.42	24.72
		O_{α}	531.1	37.88	
		O_{β}	530.35	43.7	
350	61.61	O_{ab}	532.33	6.15	16.62
		O_{α}	531.2	26.98	
		O_{β}	530.04	66.88	
500	64.67	O_{ab}	532.09	7.81	12.31
		O_{α}	531.11	19.04	
		O_{β}	530.05	73.15	
650	67.51	O_{ab}	532.59	7.33	10.55
		O_{α}	531.42	15.63	
		O_{β}	530.85	77.05	
800	68.08	O_{ab}	532.55	10.47	9.86
		O_{α}	531.3	14.48	
		O_{β}	530.18	75.05	

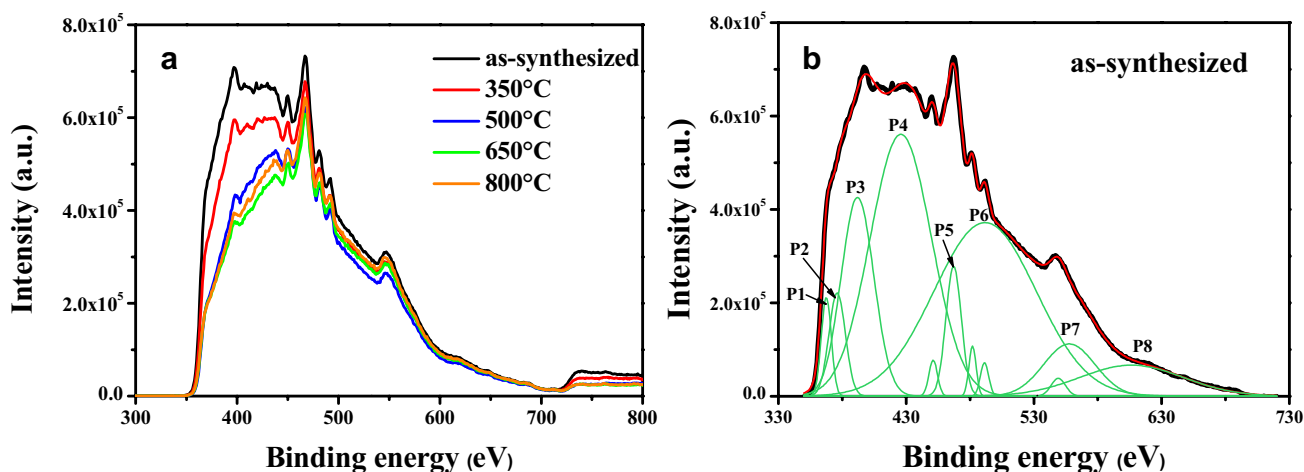


Fig. 11 **a** Room temperature PL spectra of the as-synthesized and annealed FTO NPs with different annealing temperature; **b** Gaussian deconvoluted PL spectrum of FTO NPs annealed at 500 °C

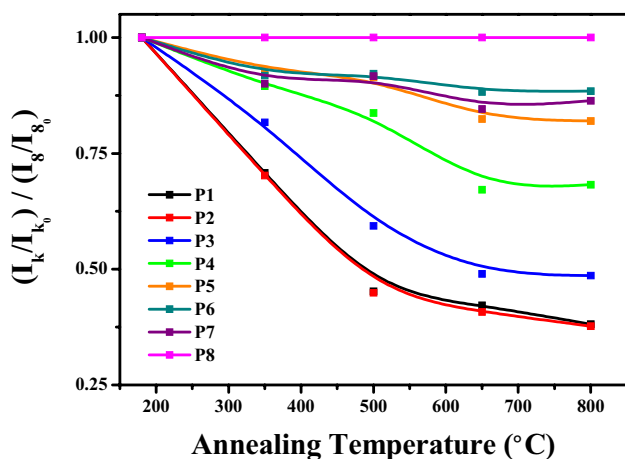


Fig. 12 The intensity changes of PL Gaussian peaks compared with Gaussian P8

charged states of oxygen vacancies are V_O^0 , V_O^+ and V_O^{++} [37]. Among these, V_O^0 is a shallow donor which lies near the conduction band. In this work, the near-band-edge (NBE) emission at 367 nm (~ 3.37 eV) can be attributed to the electron transition on the V_O^0 level to the valence band [38]. Thus, the V_O^0 energy level is located at around 0.40 eV below the conduction, which is nearly the same as that of 0.39 eV, as reported by Mrabet et al. [39]. Most of the oxygen vacancies are likely in the V_O^+ state, from which the electron transits to the valence band that gives rise to the emission peak at 426 nm (2.91 eV). The V_O^+ energy level is located at around 0.87 eV below the conduction, which is accordance with that of 0.85 eV, as we reported before [24]. V_O^{++} is acted as an acceptor that lies on 0.63 eV above the valence band, according with that of 0.65 eV, as

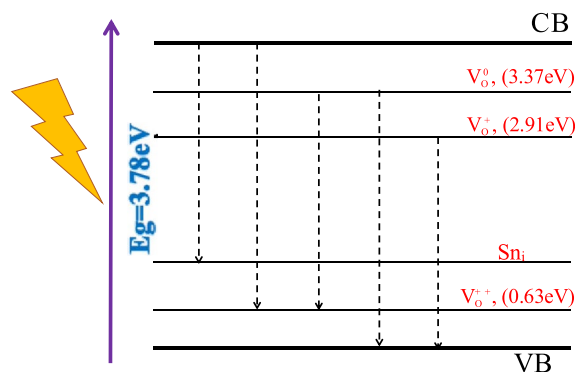


Fig. 13 The band gap diagram of FTO NPs with defect levels

we reported before [24]. And the electron transition from conduction band to it gives rise to the emission peak at 392 nm (3.16 eV). What is more, the combination of the donor–acceptor pair will produce discontinuous emission peaks in the PL spectra [40]. Therefore, the P5 and the small peaks around it could be attributed to the electron transition from the V_O^0 level to the V_O^{++} level. The schematic band diagram of FTO NPs is given in Fig. 13, within the presence of tin interstitial defect (Sn_i) to explain the green and green–red emissions (P6 ~ P8). The Sn_i level is located at 2.52 eV below the bottom of the conduction band. While, the V_O^0 and V_O^+ energy levels are located at around 0.40 eV and 0.87 eV below the conduction, respectively. The V_O^{++} energy level is located at around 0.62 eV above the valence band.

With the respect of annealing, it is found that the PL intensity decreases rapidly as the annealing temperature increases. This is attributed to the reduction of surface defects (especially oxygen vacancies) [41], caused by

occupation of oxygen vacancies lattice sites in FTO NPs by O^{2-} ions during the annealing treatment, as is shown in XPS results. The remarkable decrease in the PL intensity related to the defects with annealing strongly supports the increase of crystalline size of FTO NPs after annealed, as observed in XRD, TEM and Raman results.

3.9 Photocatalytic analysis

The photocatalytic performance of FTO NPs could be explained by the following mechanism: The UV irradiation is absorbed by FTO NPs, exciting electron transition from the valence band (VB) to the conduction band (CB), leaving same amount of holes in its VB to generate electrons–holes pairs. Generated electron–hole pairs will undergo the following three ways:

- (1) Part of the generated electron–hole pairs recombine directly in the internal of materials;
- (2) Part of the electron–hole pairs are being captured on the metastable surface, so as to make the pairs recombined on it;
- (3) Another part of the generated electron–hole pairs will transfer to the particle surface and can directly contact with surrounding solution. Electrons can react with dissolved oxygen molecules to produce superoxide anion radicals ($\bullet O_2^-$). Meanwhile, the holes can oxidize OH^- or H_2O to form hydroxyl radical ($\bullet OH$). What is more, the resulted strong oxidizing $\bullet O_2^-$ and $\bullet OH$ will thoroughly degrade organic dyes into H_2O and CO_2 .

Therefore, the competition of the generation and recombination of the electron–hole pairs has a great influence on the photocatalytic efficiency. There are basically two ways to improve the photocatalytic efficiency of SnO_2 nanostructures. First, the decrease in the electron–hole recombination rate can prolong the time to take part in the photocatalytic reaction. Second, optimizing the morphology and structure of the catalyst can get more reactive species, which has a significant effect on enhancing the photocatalytic efficiency. However, there are many factors affecting photocatalytic performance, such as particle size, specific surface area, morphology and lattice defects.

The particle size of catalyst has a great influence on its photocatalytic efficiency. As is talked above, FTO NPs annealed at lower temperature have smaller particle size and specific surface area. On the one hand, due to the small particle size, the time to transfer to the particle surface for internal generated electron–hole pairs has been shortened, which reduces the recombination rate of them. On the other hand, the larger specific surface area can increase the contact area with solution and provide more active sites for the adsorption of reagent molecules, increase the productivity

of generated electron–hole pairs, and then promote the photocatalytic activity. Surface defects are ranked among the important factors promoting the photocatalytic activity of semiconductor materials for the degradation of organic dye, which increases the surface reaction sites for harvesting generated electrons and holes. Since the defect levels are lower than the bottom of CB and higher than the top of VB, defects can act as the carries acceptor to capture generated electrons and holes. This effect promotes surface carries transfer reaction from internal of particle where electrons and holes generated to defect sites on the surface of FTO NPs, and thus the photocatalytic activity enhanced.

In this work, the as–synthesized FTO NPs shows the highest photocatalytic ability among all samples. This can be ascribed to the relative large specific surface areas, small crystallite size and highest oxygen vacancies concentration. We notice that the photocatalytic activity shows a decreasing tendency with increasing of annealing temperature up to 500 °C, and that of the 500 °C annealed FTO NPs has the lowest. This can be well understood according to the increase of grain size, and decrease of specific surface areas. In addition, subsequent annealing has been found to reduce oxygen vacancies concentration, which lowers the ability to capture electronic–hole pairs and reduce the photocatalytic activity. However, with the further increase in annealing temperature above 500 °C, the photocatalytic activity of the samples has been enhanced. This can be ascribed to the following two reasons. Firstly, the increase in size will narrow the band gap of the semiconductors (quantum size effect), which in turn favors for the separation of electron–hole pair and reduce the recombination of them in the degradation process. Secondly, the crystallization is obvious improved with higher annealing temperature, which can restrain the carries recombination, as discussed in the TEM analysis part. Therefore, it can be seen that the annealing temperature has a great effect on the photocatalytic activity of the FTO NPs.

To further clarify the possible mechanism of photocatalysis, the reactive species trapping experiments have been performed as shown in Fig. 14. In this case, 1,4-benzoquinone (BQ), ethylene diamine tetra-acetic acid disodium salt (EDTA-2Na) and isopropanol (IPA) were used as $\bullet O_2^-$, h^+ and $\bullet OH$ scavenger, respectively. When BQ is introduced, significant reduction on the photocatalytic degradation efficiency occurs, indicating $\bullet O_2^-$ is the crucial active species contributing to the degradation reaction. However, with the addition of IPA and EDTA-2Na, the degradation efficiency changes slightly, suggesting $\bullet OH$ and h^+ radicals are not the main active species in the photocatalytic system of FTO NPs. Besides, both IPA and EDTA-2Na can increase the reaction degradation efficiency slightly. This result can be explained by the following steps [42]:



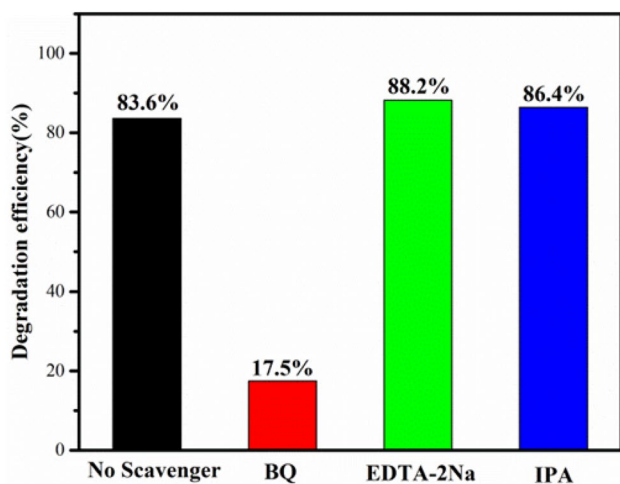
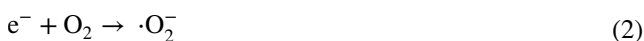


Fig. 14 Degradation efficiency of a MO solution by using different radical scavengers for as-synthesized FTO NPs under UV (40 min)



The IPA and EDTA-2Na can indirectly consume the h^+ in FTO NPs, leading more e^- in FTO NPs. Therefore, the e^- reaction with surface adsorbed oxygen molecules to form $\cdot O_2^-$, which can promote photocatalytic efficiency because $\cdot O_2^-$ is the main active species. Based on the above experimental results, a possible photocatalytic mechanism is drawn in Fig. 15.

4 Conclusion

FTO NPs were successfully synthesized through hydrothermal method with subsequent annealing process. The obvious diffraction peaks and clear lattice fringes confirmed the rutile phase of SnO_2 . The average crystalline sizes increased from 3 nm to 20 nm. As the annealing temperature increases the estimated band gaps were reduced from the 3.91 eV to 3.67 eV. The specific surface area is found to decrease with increasing annealing temperature. From the XPS measurement the binding energies of Sn 3d, O1s and F1s species were confirmed, and oxygen vacancy concentrations are found to decrease at higher annealing temperature as well. Photoluminescence (PL) spectra explored the variation of different oxygen vacancies resulting from annealing process. The as-synthesized FTO NPs showed higher photocatalytic activity decomposing dye methyl orange (MO) under UV light irradiation, owing to the larger specific surface area

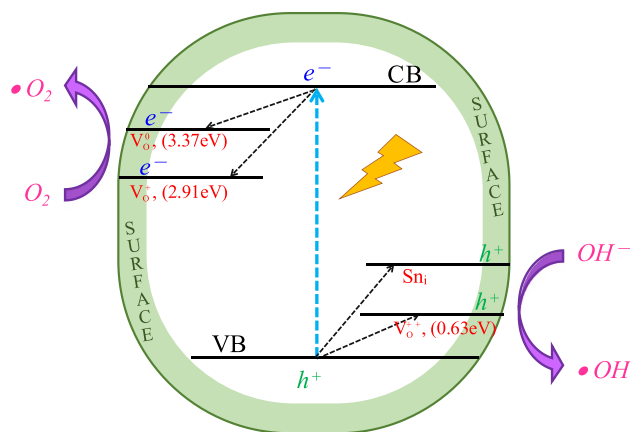


Fig. 15 Schematic illustration for the proposed mechanism of photocatalytic degradation of MO by FTO NPs

and oxygen vacancy concentration. The reactive species $\cdot O_2^-$ played the key role in MO degradation system. Photocatalytic activity of the 800 °C annealed FTO NPs are enhanced may attribute to the narrowed band gap, improved crystallization.

Acknowledgements This work was financially supported by the National Key Research and Development Program of China (2016YFB0303902), National Natural Science Foundation of China (No. 51602278), Natural Science Foundation of Hebei Province (No. E2016203149), the Key Basic Research Project of Hebei Province (No. 17961109D) and Hebei Province Department of Higher Education Science and Technology Plan of Young Talents (No. BJ2018004).

References

- C. Kilic, A. Zunger, Origins of coexistence of conductivity and transparency in SnO_2 . *Phys. Rev. Lett.* **88**, 95501 (2002). <https://doi.org/10.1103/PhysRevLett.88.095501>
- R. Godin, B.D. Sherman, J.J. Bergkamp, C.A. Chesta, A.L. Moore, T.A. Moore, R.E. Palacios, G. Cosa, Charge-transfer dynamics of fluorescent dye-sensitized electrodes under applied biases. *J. Phys. Chem. Lett.* **6**, 2688–2693 (2015). <https://doi.org/10.1021/acs.jpcllett.5b01061>
- J. Guo, J. Zhang, H. Gong, D. Ju, B. Cao, Au nanoparticle-functionalized 3D SnO_2 microstructures for high performance gas sensor. *Sens. Actuators B* **226**, 266–272 (2016). <https://doi.org/10.1016/j.snb.2015.11.140>
- Y. Li, W. Yin, R. Deng, R. Chen, J. Chen, Q. Yan, B. Yao, H. Sun, S. Wei, T. Wu, Realizing a SnO_2 -based ultraviolet light-emitting diode via breaking the dipole-forbidden rule. *NPG Asia Mater.* **4**, e30 (2012). <https://doi.org/10.1038/am.2012.56>
- H. Ye, Z. Liu, X. Liu, B. Sun, X. Tan, Y. Tu, T. Shi, Z. Tang, G. Liao, 17.78% efficient low-temperature carbon-based planar perovskite solar cells using Zn-doped SnO_2 electron transport layer. *Appl. Surf. Sci.* **478**, 417–425 (2019). <https://doi.org/10.1016/j.apsusc.2019.01.237>
- M.T. Uddin, Y. Nicolas, C. Olivier, T. Toupance, L. Servant, M.M. Müller, H. Kleebe, J. Ziegler, W. Jaegermann, Nanostructured SnO_2 -ZnO heterojunction photocatalysts

- showing enhanced photocatalytic activity for the degradation of organic dyes. *Inorg. Chem.* **51**, 7764–7773 (2012). <https://doi.org/10.1021/ic300794j>
7. B. Babu, A.N. Kadam, R.V.S.S. Ravikumar, C. Byon, Enhanced visible light photocatalytic activity of Cu-doped SnO₂ quantum dots by solution combustion synthesis. *J. Alloy. Compd.* **703**, 330–336 (2017). <https://doi.org/10.1016/j.jallcom.2017.01.311>
 8. V. Etacheri, G.A. Seisenbaeva, J. Caruthers, G. Daniel, J. Nedelec, V.G. Kessler, V.G. Pol, Ordered network of interconnected SnO₂ nanoparticles for excellent lithium-ion storage. *Adv. Energy Mater.* **5**, 1401289 (2015). <https://doi.org/10.1002/aenm.201401289>
 9. S. Pan, S. Wang, Y. Zhang, S. Xu, F. Kong, Y. Luo, Y. Tian, X. Teng, G. Li, Surface Fe³⁺-decorated pristine SnO₂ nanoparticles with enhanced ·OH radical generation performance. *Catal. Commun.* **24**, 96–99 (2012). <https://doi.org/10.1016/j.catcom.2012.03.034>
 10. M. Zhang, T. An, X. Hu, C. Wang, G. Sheng, J. Fu, Preparation and photocatalytic properties of a nanometer ZnO–SnO₂ coupled oxide. *Appl. Catal. A* **260**, 215–222 (2004). <https://doi.org/10.1016/j.apcata.2003.10.025>
 11. H. Ma, C. Li, J. Yin, X. Pu, D. Zhang, C. Su, X. Wang, X. Shao, Polyoxometalate enhances the photocatalytic performance of poly-aniline/SnO₂ composites. *Mater. Lett.* **168**, 103–106 (2016). <https://doi.org/10.1016/j.matlet.2016.01.041>
 12. Y. Yang, X. Yang, D. Leng, S. Wang, W. Zhang, Fabrication of g-C₃N₄/SnS₂/SnO₂ nanocomposites for promoting photocatalytic reduction of aqueous Cr(VI) under visible light. *Chem. Eng. J.* **335**, 491–500 (2018). <https://doi.org/10.1016/j.cej.2017.10.173>
 13. J. Wei, S. Xue, P. Xie, R. Zou, Synthesis and photocatalytic properties of different SnO₂ microspheres on graphene oxide sheets. *Appl. Surf. Sci.* **376**, 172–179 (2016). <https://doi.org/10.1016/j.apsusc.2016.03.058>
 14. J. Mazloom, F.E. Ghodsi, H. Golmoghjeh, Synthesis and characterization of vanadium doped SnO₂ diluted magnetic semiconductor nanoparticles with enhanced photocatalytic activities. *J. Alloy Compd.* **639**, 393–399 (2015). <https://doi.org/10.1016/j.jallcom.2015.03.184>
 15. L. Yang, J. Huang, L. Shi, L. Cao, W. Zhou, K. Chang, X. Meng, G. Liu, Y. Jie, J. Ye, Efficient hydrogen evolution over Sb doped SnO₂ photocatalyst sensitized by Eosin Y under visible light irradiation. *Nano Energy* **36**, 331–340 (2017). <https://doi.org/10.1016/j.nanoen.2017.04.039>
 16. G. Caputo, S.G. Leonardi, S. Mariotti, M. Latino, N. Donato, S. Trocino, N. Pinna, G. Neri, Microstructural, electrical and hydrogen sensing properties of F-SnO₂ nanoparticles. *Procedia Eng.* **87**, 1087–1090 (2014). <https://doi.org/10.1016/j.proeng.2014.11.353>
 17. Y. Zang, L. Li, X. Li, R. Lin, G. Li, Synergistic collaboration of g-C₃N₄/SnO₂ composites for enhanced visible-light photocatalytic activity. *Chem. Eng. J.* **246**, 277–286 (2014). <https://doi.org/10.1016/j.cej.2014.02.068>
 18. T. Jia, W. Wang, F. Long, Z. Fu, H. Wang, Q. Zhang, Synthesis, characterization, and photocatalytic activity of Zn-doped SnO₂ hierarchical architectures assembled by nanocones. *J. Phys. Chem. C* **113**, 9071–9077 (2009). <https://doi.org/10.1021/jp9021272>
 19. Z. Wen, G. Wang, W. Lu, Q. Wang, Q. Zhang, J. Li, Enhanced photocatalytic properties of mesoporous SnO₂ induced by low concentration ZnO doping. *Cryst. Growth Des.* **7**, 1722–1725 (2007). <https://doi.org/10.1021/cg060801z>
 20. A. Ahmed, M. Naseem Siddique, U. Alam, T. Ali, P. Tripathi, Improved photocatalytic activity of Sr doped SnO₂ nanoparticles: a role of oxygen vacancy. *Appl. Surf. Sci.* **463**, 976–985 (2019). <https://doi.org/10.1016/j.apsusc.2018.08.182>
 21. L. Yang, Y. Yang, T. Liu, X. Ma, S.W. Lee, Y. Wang, Oxygen vacancies confined in SnO₂ nanoparticles for glorious photocatalytic activities from the UV, visible to near-infrared region. *New J. Chem.* **42**, 15253–15262 (2018). <https://doi.org/10.1039/C8NJ00668G>
 22. H. Kim, R.C.Y. Auyeung, A. Piqué, Transparent conducting F-doped SnO₂ thin films grown by pulsed laser deposition. *Thin Solid Films* **516**, 5052–5056 (2008). <https://doi.org/10.1016/j.tsf.2007.11.079>
 23. M. Zhou, J. Yu, S. Liu, P. Zhai, L. Jiang, Effects of calcination temperatures on photocatalytic activity of SnO₂/TiO₂ composite films prepared by an EPD method. *J. Hazard. Mater.* **154**, 1141–1148 (2008). <https://doi.org/10.1016/j.jhazmat.2007.11.021>
 24. X. Wang, X. Wang, Q. Di, H. Zhao, B. Liang, J. Yang, Mutual effects of fluorine dopant and oxygen vacancies on structural and luminescence characteristics of F doped SnO₂ nanoparticles. *Materials* **10**, 1398 (2017). <https://doi.org/10.3390/ma10121398>
 25. A. Azam, A.S. Ahmed, S.S. Habib, A.H. Naqvi, Effect of Mn doping on the structural and optical properties of SnO₂ nanoparticles. *J. Alloy Compd.* **523**, 83–87 (2012). <https://doi.org/10.1016/j.jallcom.2012.01.072>
 26. J. Kaur, J. Shah, R.K. Kotnala, K.C. Verma, Raman spectra, photoluminescence and ferromagnetism of pure, Co and Fe doped SnO₂ nanoparticles. *Ceram. Int.* **38**, 5563–5570 (2012). <https://doi.org/10.1016/j.ceramint.2012.03.075>
 27. M. Shohel, M.S. Miran, M.A.B.H. Susan, M.Y.A. Mollah, Calcination temperature-dependent morphology of photocatalytic ZnO nanoparticles prepared by an electrochemical–thermal method. *Res. Chem. Intermed.* **42**, 5281–5297 (2016). <https://doi.org/10.1007/s11164-015-2358-x>
 28. Y. Song, J. Gu, K. Xia, J. Yi, H. Chen, X. She, Z. Chen, C. Ding, H. Li, H. Xu, Construction of 2D SnS₂/g-C₃N₄ Z-scheme composite with superior visible-light photocatalytic performance. *Appl. Surf. Sci.* **467–468**, 56–64 (2019). <https://doi.org/10.1016/j.apsusc.2018.10.118>
 29. R. Huang, S. Huang, D. Chen, Q. Zhang, T. Le, Q. Wang, Z. Hu, Z. Chen, Y. Jiang, B. Zhao, Insight into efficient pollutant degradation from paramorphic SnO₂ hierarchical superstructures. *J. Alloy Compd.* **776**, 287–296 (2019). <https://doi.org/10.1016/j.jallcom.2018.10.289>
 30. S. Monticone, R. Tufeu, A.V. Kanaev, E. Scolan, C. Sanchez, Quantum size effect in TiO₂ nanoparticles: does it exist? *Appl. Surf. Sci.* **162**, 565–570 (2000). [https://doi.org/10.1016/S0169-4332\(00\)00251-8](https://doi.org/10.1016/S0169-4332(00)00251-8)
 31. P. Sun, L. You, Y. Sun, N. Chen, X. Li, H. Sun, J. Ma, G. Lu, Novel Zn-doped SnO₂ hierarchical architectures: synthesis, characterization, and gas sensing properties. *CrystEngComm* **14**, 171–178 (2012). <https://doi.org/10.1039/c1ce06197f>
 32. N. Li, K. Du, G. Liu, Y. Xie, G. Zhou, J. Zhu, F. Li, H. Cheng, Effects of oxygen vacancies on the electrochemical performance of tin oxide. *J. Mater. Chem. A* **1**, 1536–1539 (2013). <https://doi.org/10.1039/C2TA01012G>
 33. Talinungsang, D. Dhar Purkayastha, M.G. Krishna, Dopant controlled photoinduced hydrophilicity and photocatalytic activity of SnO₂ thin films. *Appl. Surf. Sci.* **447**, 724–731 (2018). <https://doi.org/10.1016/j.apsusc.2018.04.028>
 34. Y. Zhao, J. Liu, Q. Liu, Y. Sun, D. Song, W. Yang, J. Wang, L. Liu, One-step synthesis of SnO₂ hollow microspheres and its gas sensing properties. *Mater. Lett.* **136**, 286–288 (2014). <https://doi.org/10.1016/j.matlet.2014.08.073>
 35. S.A. Hejazi Juybari, H. Milani Moghaddam, Facile fabrication of porous hierarchical SnO₂ via a self-degraded template and their remarkable photocatalytic performance. *Appl. Surf. Sci.* **457**, 179–186 (2018). <https://doi.org/10.1016/j.apsusc.2018.06.259>
 36. F. Arlinghaus, Energy bands in stannic oxide (SnO₂). *J. Phys. Chem. Solids* **35**, 931–935 (1974). [https://doi.org/10.1016/S0022-3697\(74\)80102-2](https://doi.org/10.1016/S0022-3697(74)80102-2)
 37. C. Lu, J. Wang, F. Xu, A. Wang, D. Meng, Zn-doped SnO₂ hierarchical structures formed by a hydrothermal route with remarkably

- enhanced photocatalytic performance. *Ceram. Int.* **44**, 15145–15152 (2018). <https://doi.org/10.1016/j.ceramint.2018.05.151>
38. T. Li, X. Zhang, J. Ni, J. Fang, D. Zhang, J. Sun, C. Wei, S. Xu, G. Wang, Y. Zhao, Modify the Schottky contact between fluorine-doped tin oxide front electrode and p-a-SiC: H by carbon dioxide plasma treatment. *Sol. Energy* **134**, 375–382 (2016). <https://doi.org/10.1016/j.solener.2016.04.042>
39. C. Mrabet, A. Boukhachem, M. Amlouk, T. Manoubi, Improvement of the optoelectronic properties of tin oxide transparent conductive thin films through lanthanum doping. *J. Alloy. Compd.* **666**, 392–405 (2016). <https://doi.org/10.1016/j.jallcom.2016.01.104>
40. F. Gu, S.F. Wang, M.K. Lü, G.J. Zhou, D. Xu, D.R. Yuan, Photoluminescence properties of SnO₂ nanoparticles synthesized by sol–gel method. *J. Phys. Chem. B* **108**, 8119–8123 (2004). <https://doi.org/10.1021/jp036741e>
41. L.Z. Liu, J.Q. Xu, X.L. Wu, T.H. Li, J.C. Shen, P.K. Chu, Optical identification of oxygen vacancy types in SnO₂ nanocrystals. *Appl. Phys. Lett.* **102**, 31916 (2013). <https://doi.org/10.1063/1.4789538>
42. G. Di, Z. Zhu, H. Zhang, J. Zhu, Y. Qiu, D. Yin, S. Küppers, Visible-light degradation of sulfonamides by Z-scheme ZnO/g-C₃N₄ heterojunctions with amorphous Fe₂O₃ as electron mediator. *J. Colloid Interface Sci.* **538**, 256–266 (2019). <https://doi.org/10.1016/j.jcis.2018.11.100>

Publisher's Note Springer Nature remains neutral with regard to jurisdictional claims in published maps and institutional affiliations.